# Development of a Low-Cost Fine Steering Mirror

Steven R. Wassom and Morgan Davidson*

**Abstract**

The Space Dynamics Laboratory has used internal funds to develop a prototype low-cost two-axis fine steering mirror (FSM) for space-based and airborne applications. The FSM has a lightweight 75 mm-by-150-mm high-reflectance mirror, high angular deflection capability for along-track ground motion compensation and cross-track pointing, and a 70-Hertz bandwidth for small amplitudes to help cancel unwanted jitter. It makes use of off-the-shelf components as much as possible. Key performance parameters are: Clear aperture, 75 mm; elevation angle, ±15 deg (mechanical); azimuth angle, ±60 deg (mechanical); slew rate, greater than 75 deg/sec; bandwidth, 70 Hz; steady-state average error, about 1 arcsec; average power dissipation, 0.4 Watts; mirror surface, figure, <0.1 waves RMS; and total mechanical mass, 1 kg. Key components for the elevation axis include a rotary voice coil and a unique patent-pending non-contact feedback sensor. The azimuth axis features a brushless DC motor and a high-resolution optical encoder. Rapid prototyping, autocoding, and real-time hardware-in-the-loop (HIL) testing were used to develop the control algorithms. Additional accomplishments include temperature mapping of the feedback sensor, inventing a successful passive launch lock, launch vibration testing, and subjecting the system to a space-like environment at pressures down to 1e-7 torr and temperatures down to 164 K.

## Introduction

Over the past two years, Space Dynamics Laboratory (SDL) has used internal funds to develop a prototype low-cost two-axis fine steering mirror (FSM). This mechanism is intended to have a broad flexibility for both space-based and airborne applications.

The main purpose of this effort was to reduce the cost of a normally expensive technology while maintaining performance, thus enabling this capability for more applications. A $2 million price tag has not been uncommon. The first year's development effort required about $200,000 and resulted in a successful working prototype (Ref. 1).

This report will review the accomplishments of the first year and describe the additional progress of the second year that includes:

- Subjecting the system to a space-like environment at pressures down to 1e-7 torr and temperatures down to 164 K
- Verifying that the system will survive a typical launch vibration test profile
- Performing temperature mapping of the patent-pending feedback sensor
- Inventing a successful passive launch lock
- Mounting the system on a portable cart for demonstrations

**Figure 1. Prototype FSM**

* Space Dynamics Laboratory / Utah State University Research Foundation, North Logan, Utah

## General Requirements

Although this FSM was not intended for a specific program, some general top-level requirements and performance goals were established. An angular position accuracy of about 1-2 arcsec was desired to minimize jitter. A clear aperture of 75 mm was chosen as a good starting point, with the intention that the design be scalable to larger or smaller apertures. An elevation axis deflection of ±15 deg (mechanical) was chosen to perform ground motion compensation (GMC) along the flight path, and the azimuth axis deflection was chosen to be ±60 deg to achieve both off-track pointing and the ability to rotate far enough to view an on-board calibration source. A high bandwidth approaching 70-100 Hz was desired to enable jitter control during pointing and scanning.

The final performance parameters achieved are tabulated in the section below describing the test results.

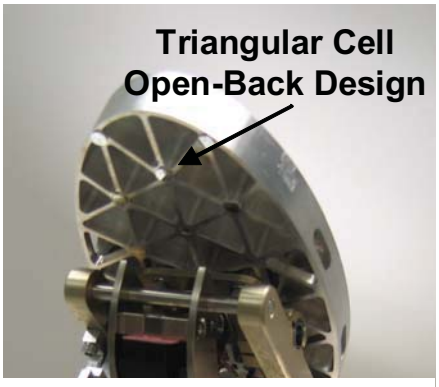


**Figure 2. Back View of Mirror Showing Triangular Rib Structure**

## Design Description

Mirror Design

To meet the aperture and bandwidth goals, the mirror needed to be lightweight and low cost. Mirror trades included several materials (Be, Al, SiC) and shaft connections (bonded, bolted, or integral). The final selection was a lightweighted Al mirror to keep costs low, and a bolted connection to facilitate future design changes.

The flat mirror geometry provides a 75-mm aperture when scanned to a 60-deg optical angle (30-deg mechanical angle). The flat mirror is elliptical with a 75-mm-by-150-mm clear aperture. Thermal considerations coupled with the light-weighting requirement for high bandwidth necessitated the open back form shown in Figure 2, which provides a 60% reduction in mass compared with a solid mirror. Total mirror mass is 0.16 kg corresponding with a 17 kg/m$^2$ optical surface area mirror density.

Triangular cells were selected over hexagonal or square cells as they are considered to be the optimum cell geometry (Ref. 2). Triangular cells also work well in providing a uniform distribution of ribs across the part and structure for mounting features.

The mirror is mounted on four flexure-isolated pads in the center of the mirror back. The mounting pads require flexure isolation to reduce mounting distortion of the optical surface; however, the stiffness of the flexures must balance mounting distortion isolation and mirror modal response. Finite element analysis was used to find the optimum performance balance for the scan mirror application.

Mirror Surface Finish

The mirror surface is fabricated using single point diamond turning (SPDT) combined with post-polishing. An RMS surface roughness better than 20 angstroms is obtained utilizing a post-polishing method termed VQ for “Visible Quality”. This process aids in the removal of the grooves typical from SPDT.

The RMS surface figure of the mounted mirror was measured to be near 1/12 wave HeNe at 210K. This shows the capability of this mirror to hold good optical figure. Test and analysis results are discussed in detail later in the paper. Table 1 summarizes the optical performance specifications.

**Table 1. Mirror Optical Performance Specifications**

| Description | Specification |
|---|---|
| Mirror Mass | 0.16 kg |
| Operating Temperature | 210K |
| Optical Aperture @60 deg Optical Angle | 75 mm |
| RMS Surface Figure | < 1/10 waves HeNe |
| RMS Surface Roughness | < 20 angstroms |

Elevation Axis

For the elevation axis bearing, options considered were flexures, flexural pivots, and conventional ball bearings. Flexural pivots were chosen based on their high deflection capability, negligible friction, and SDL's extensive experience with these devices in their Michelson interferometer.

Actuator choices for the elevation axis included piezo actuators, magnetostrictive actuators, voice coils, brushless DC motors, and stepper motors. A rotary voice coil was chosen primarily for its favorable ratio of rotation angle to package size, since only a limited rotation was required. Other advantages to the rotary voice coil are simplicity, low cost, and high bandwidth potential.

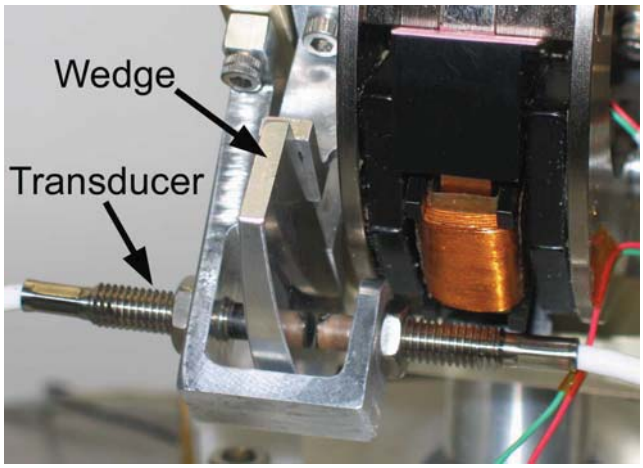


**Figure 3. Close-up of Wedge Sensor, Showing Precision Wedge and Displacement Transducers**

The moving coil of the elevation axis and the mirror are bolted to a mirror mount, which is supported on flexural pivots. The pivots and the voice coil magnets are mounted to a compact U-shaped yoke. The mounting scheme for the pivots is the same that is used in SDL's Michelson interferometers. The pivots were sized to support the rotating mass without failure during a representative launch load and to ensure virtually infinite life during on-orbit duty cycles.

The feedback sensor for the elevation axis was selected from the following options: non-contact proximity transducers (inductive or capacitive), strain gages, optical encoders, resolvers, and inductosyns. Inductive non-contact sensors were chosen for their low weight, compact packaging, low cost, high resolution, and SDL's related experience.

The feedback device for the elevation axis is unique and patent-pending. In this angular measurement device (called the wedge sensor), two non-contact inductive displacement transducers are arranged in opposition facing a moving target wedge made of aluminum (see Figure 3). These transducers exhibit excellent resolution and repeatability over a limited range. The precision wedge extends the range of the non-contact transducers by converting angular motion to limited linear motion. Using two opposed transducers minimizes the sensitivity of the device to relative displacements out of the plane of symmetry of the wedge (wobble, vibration, misalignments, etc). Nonlinearity in the wedge sensor over the large deflection angles was mapped using a theodolite. This map was incorporated into the elevation axis control algorithm.

Azimuth Axis

The azimuth axis requires much larger deflections and needs to move a larger inertia. Consequently, the bearing trades were more limited. Ball bearings were chosen due to their extensive heritage in space and SDL's experience base. Actuator options were brushless DC motors and stepper motors. Brushless DC was chosen for its high bandwidth and accuracy capabilities and typically long service life. Feedback device options were encoders, resolvers, and inductosyns. An optical encoder was chosen for high accuracy, low mass, and related experience.

The output shaft of the motor is connected to the yoke supporting the elevation axis. The optical encoder has a resolution of 4.5 arcsec per count. Although this drive system is not designed for space, it uses the same type of components as another SDL scan mirror drive system, which has been operating flawlessly for over six years in orbit. Upgrading the azimuth axis to space-worthiness has low risk.

Electronics

Two independent sets of electronics are used to drive the azimuth and elevation motors. The azimuth motor is driven using a commercial linear brushless servo amplifier. The elevation motor uses a simple amplifier circuit based on an operational amplifier.

## Structural/Thermal Analysis

Mirror Modal Analysis

Finite Element Analysis (FEA) was used to predict the modes of the mirror. The high control system bandwidth near 70 Hz required the mirror modes to be considerably higher.

A normal modes analysis was run. Table 2 lists the mode shape descriptions. Figure 4 depicts the first mode: a torsional mode about the Z-axis at 270 Hz. The majority of the deformation and strain energy is in the flexure mount.


**Figure 4. Mirror Mode 1, Torsional about Z-Axis, 270 Hz**

Mirror Mounting Distortion Predictions

Some wave-front error (WFE) is caused when non-flat surfaces are mated together with a bolt preload, producing strain in the mated parts. FEA was again used to predict optical surface displacement.

The analysis assumed that the combined worst-case flatness tolerance of the two mating surfaces produces a Z-axis forced displacement of the mounting surface. The mounting pads on the mirror have a coplanarity requirement of 2 µm. The mating surface is assumed to have a coplanarity or flatness of 12.7 µm. Conventional machining can get surfaces as good as 7.6 µm in flatness. This approach conservatively assumes that all the strain occurs in the mirror as if it were mated to an infinitely stiff part.

**Table 2. Mirror Modes Summary**

| Mode Shape Number/Description | | Frequency (Hz) |
|---|---|---|
| 1 | Mirror torsional, about Z-axis | 270 |
| 2 | Mirror rocking, about Y-axis | 390 |
| 3 | Mirror vertical or Z-direction translation, with mirror bending (saddle mode) | 1230 |
| 4 | Complex X-direction side to side translation with mirror surface bending/waves | 2700 |
| 5 | Complex Y-direction side-to-side translation with mirror surface bending/waves | 2900 |
| 6 | Second saddle mode | 3100 |

Optical surface deformations from each of the enforced displacements are then transformed into surface normal interferometric space using Zernike polynomial fitting. Piston and tilt can then be subtracted, resulting in WFE due to mounting distortion. The results show that distortion in the mirror is dominated by astigmatism and tetrafoil. Predicted surface normal displacements are shown in Figure 5 with the dominant aberrations identified in Table 3.

Mirror Thermal Elastic Predictions

Thermal simulation of the FSM in a representative orbit was used to evaluate expected performance. For the simulation, the representative orbit was a nadir-pointing low-Earth orbit. A typical baffle geometry was assumed. Standard minimum and maximum values were used for long-wave infrared heat from the earth and for reflected sunshine. Diurnal temperature profiles for the system as well as a detailed mapping of temperature variation across the face of the mirror were the principle outputs from the thermal simulation.

**Table 3. Zernike Polynomial Coefficients Ordered by Highest Contributor**

| Standard Zernike No. | Zernike Description | RMS WFE (waves HeNe) |
|---|---|---|
| 14 | Second order Astigmatism y | 0.018 |
| 6 | First order Astigmatism y | 0.017 |
| 27 | Second order Tetrafoil y | 0.005 |
| 26 | Third order Astigmatism y | 0.005 |

**Table 4. Results of Thermal Analysis**

| | Units | Case 1 | Case 2 | Case 3 |
|---|---|---|---|---|
| Azimuth motor / yoke isolation | W/K | 0.019 | 0.007 | 0.007 |
| Baffle temperature | K | 160 | 160 | 180 |
| Average mirror temperature | K | 210 | 201 | 210 |
| Mirror face gradient | K | 0.11 | 0.08 | 0.07 |
| Mirror face distortion Z-dir* | nm | 43 | 27 | 22 |

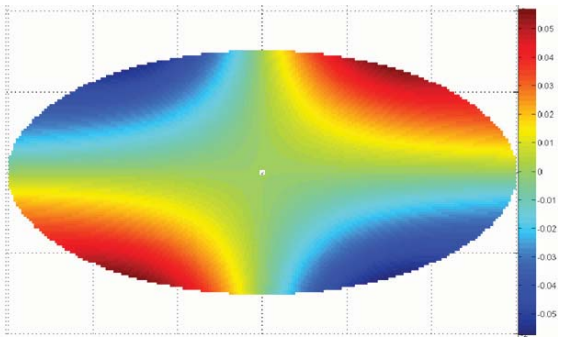

**Figure 5. Predicted Surface Normal Deformations**

Thermal analysis results showed the two most sensitive elements of the thermal design were the level of thermal isolation between the yoke and the azimuth motor and the baffle temperature. These parameters were the principle drivers in determining the operational temperature of the mirror. Because the gradients across the mirror are affected by the overall mirror temperature, the optical distortion was weakly coupled to the same parameters, showing small changes as the mirror temperature and baffle temperature varied. Table 4 shows various amounts of isolation and baffle temperatures and the resulting mirror temperature and optical distortion. A typical diurnal temperature profile during one orbit and the resulting thermal gradients across the mirror face are shown in Figure 6.

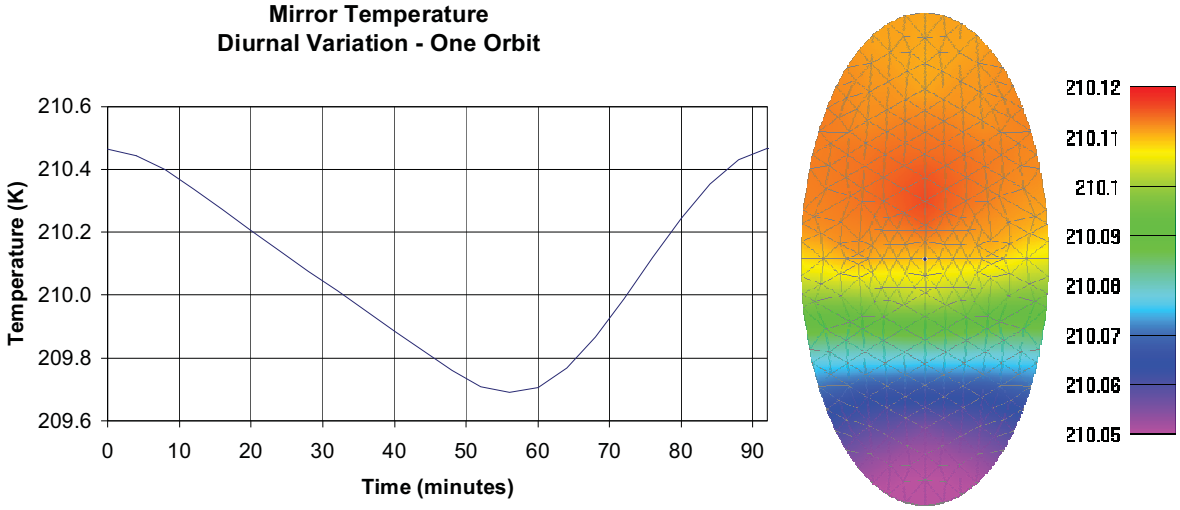


**Figure 6. Typical diurnal temperature profile (left) and thermal gradients across mirror face (right)**

FEA was again used to predict elastic distortion caused by thermal gradients across the mirror during operation in space. Coefficient of thermal expansion (CTE) mismatch at the mounting interfaces has no impact given that the mating materials are aluminum.

The thermal elastic analysis predicts a peak-to-valley sag (Z axis on a flat mirror) of 22 nm or 0.034-wave HeNe (see Figure 7). This distortion is very small and should not be a factor in maintaining a good optical figure in operation.

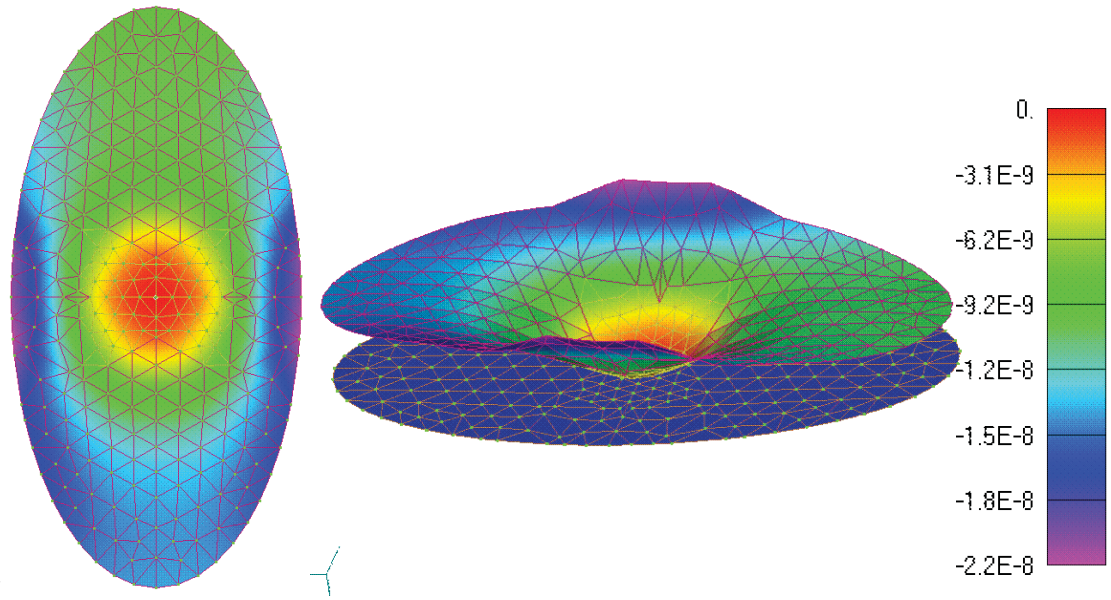


**Figure 7. Sag (meters) of Optical Surface due to Thermal Elastic Deformation**

## Control System Development

Instead of following a traditional waterfall or serial development process for the elevation and azimuth closed-loop control algorithms, SDL used the Rapid Prototyping Methodology (RPM) spiral development process shown in Figure 8. This process can be quickly iterated due to its software-driven nature. Customized features for line-of-sight (LOS) optical pointing systems include: integrated end-to-end modeling, co-simulation, and 3-D visualization of structural and system dynamics, controls, and optics; automatic C-code synthesis from block diagrams; real-time hardware-in-the-loop (HIL) testing; dynamic automated ray tracing, and a customizable GUI to monitor testing and change control parameters "on the fly." Eventually, the block diagram transforms from a virtual model of the system to the complete integrated assembly. The control algorithm is then embedded in the actual computer.

The advantages of RPM include:

- virtually no software written by hand (except for occasional device drivers)
- substantial savings of time and money in code generation
- short iteration cycles that result in early problem identification and solution
- changes can be made early in the design cycle at the component level

The left side of Figure 9 shows the multi-body dynamic model of the FSM. This high-fidelity model includes flexible- and rigid-body representations of all major components (mirror, mirror flexure, flex pivots, actuators, etc.). The right side of Figure 9 shows the top-level hierarchy of the block diagram simulation of the FSM control system with the dynamic model embedded for co-

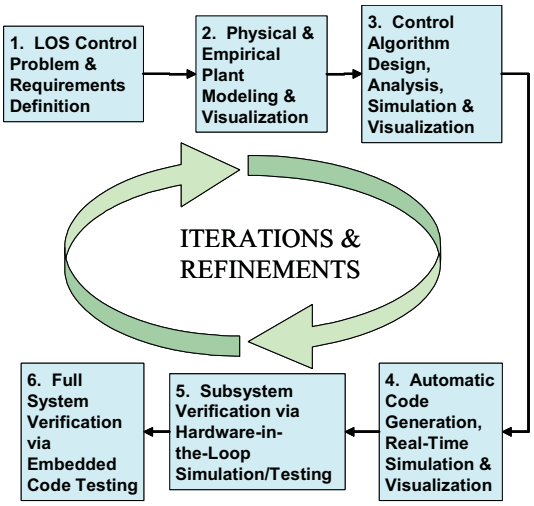


**Figure 8. SDL's RPM for Control Systems**

simulation. Each of the blocks shown has detailed algorithms and calculations within it. Analytical tools in the software were used to determine the control gains, shape the open- and closed-loop responses, and simulate the step response and frequency response.

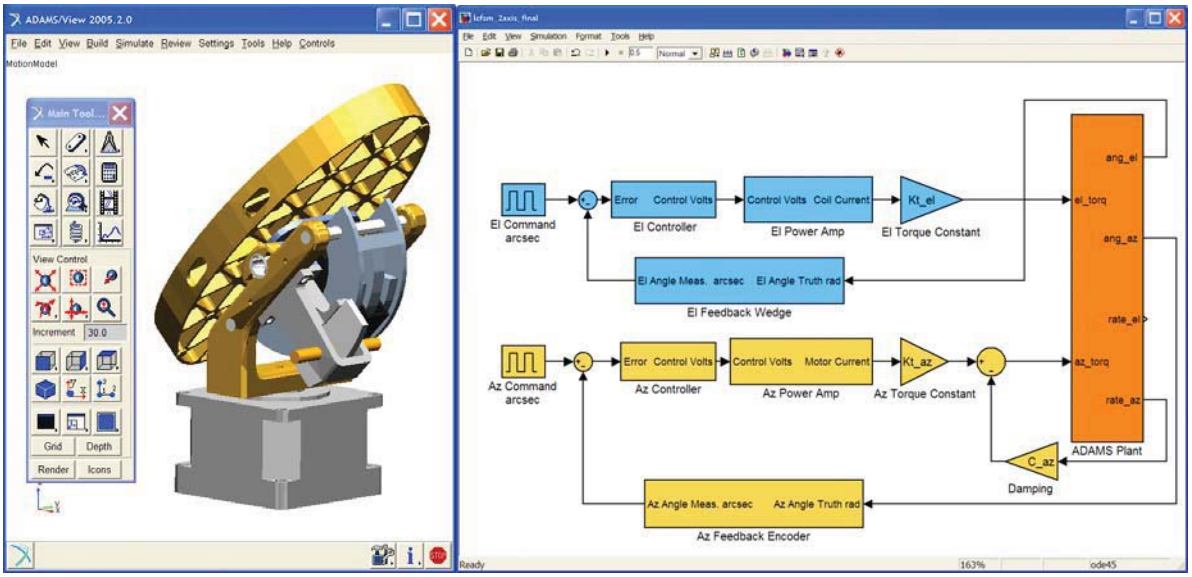


**Figure 9. FSM Dynamic Model**

## Test Results and Model Validation

Mirror Surface Figure Testing

Surface figure tests were performed on the mirror to better understand the optical performance and validate the predictions. Mounting distortion and thermal elastic distortion at cryogenic temperatures were tested using a commercial Zygo Fizeau interferometer.

The test setup (see Figure 10) consisted of mounting the mirror in a bell jar test chamber on an optical bench. The mirror is insulated and baffled to reduce thermal gradients during testing. The mirror looks out the bell jar window. The interferometer is set up to view the test mirror through a fold mirror. The fold mirror is necessary to adjust tilt on the mirror, as it is very difficult to move the large bell jar or the interferometer in fine increments.

It should be noted when viewing the test results that the interferometer only spans 100 mm of the 150 mm elliptical test mirror aperture. The test mirror aperture outside the 100-mm center was tested separately with the results showing a more behaved WFE. Also, WFE from the fold mirror was not removed from any of the results.

Room temperature tests were performed with various mounting torques applied to the mirror. The interferometric results show very little distortion from mounting. Figure 11 shows the WFE after applying 0.68 N·m to the number 4 screws. The RMS WFE error is essentially 0.025 waves HeNe with or without the applied torque. The circular grooves noticeable in the interferogram are residual SPDT marks in the

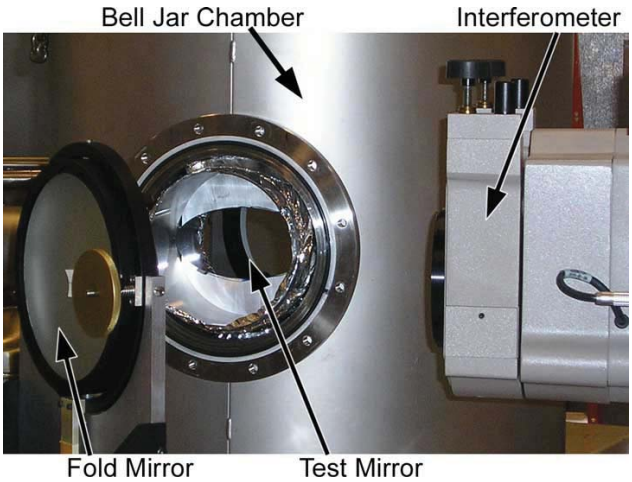


**Figure 10. Mirror Surface Figure Test Setup**

mirror. The polishing house is confident that these marks can be polished out of future mirrors.

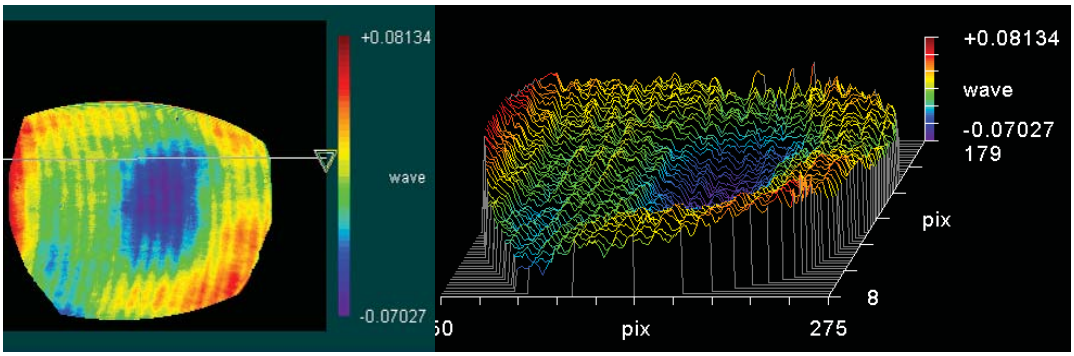


**Figure 11. Mounting Distortion Test, 0.68 N·m Torque Applied**

The mirror was then cooled with liquid nitrogen. Testing the mirror over temperature showed that WFE is dominated by the CTE mismatch of the VQ coating and the aluminum substrate producing bending in the mirror at the low cryogenic temperatures. The aluminum shrinks more at cold temperatures due to its larger CTE producing a slightly convex mirror. This bimetallic bending is much less than is typically seen with nickel-plated mirrors. Figure 12 shows how the mirror shape changed from concave at 292K to convex at 186K. RMS WFE error measured at 292K and 186K were 0.039 and 0.106 waves HeNe respectively.

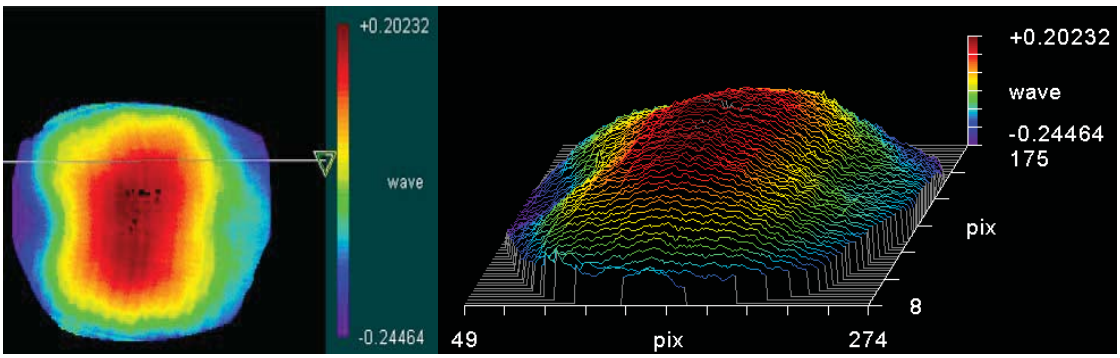


**Figure 12. Interferometric Measurements at 186K**

Figure 13 shows the RMS, PV, and Power WFE from 292K to 141K. Using this data, the RMS WFE at the required operating temperature of 210K is linearly interpolated to be nearly 0.083-wave HeNe.

The mirror retained a very good figure at 141K with a deformation shape nearly identical to the 186K measurement and a 0.125-wave RMS WFE. At temperatures lower than 141K, the WFE did not increase noticeably. Wave front measurements were measured as low as 92K with very similar performance as seen at 141K. Transient thermal gradients affected the accuracy of this data. Quilting or rib print-through was not detectable in the testing, even at temperatures as low as 92K. The mirror does however show substantial high order WFE.

The mirror surface figure exhibits great stability under mounting and cryogenic temperatures with some expected and very small bimetallic bending of the optical surface. At the 210K operating temperature the RMS WFE is near 0.083-wave HeNe.

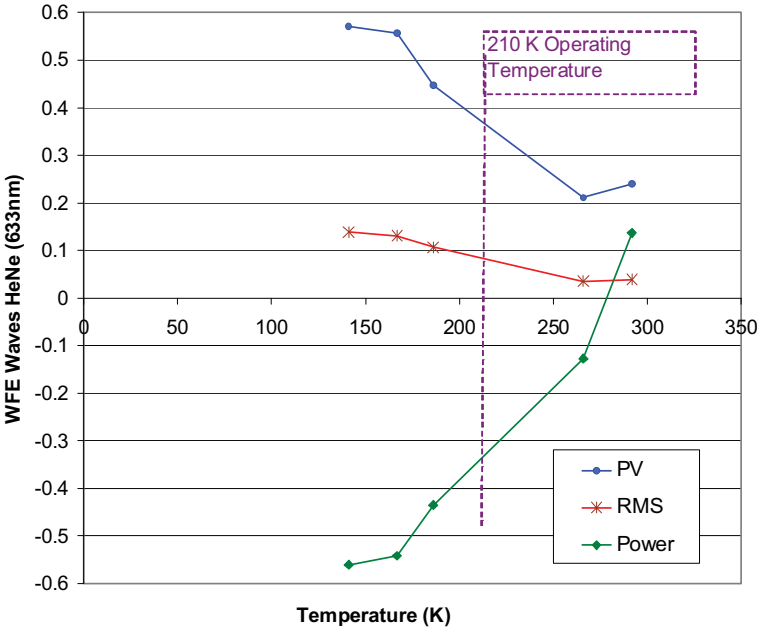


**Figure 13. Mirror WFE at Cryogenic Temperatures**

Control System Performance Testing

Considerable testing was performed to quantify the control system performance. The real-time HIL tools of the RPM process were used to test and optimize the control laws for both the elevation and azimuth control loops. A graphical block diagram was used to monitor the performance and change the control parameters "on the fly" as the tests were running.

Tests performed included large and small steps, and small-angle frequency response. The frequency response tests were performed using a control systems analyzer, which excited each axis with a sine sweep of 100 arcsec amplitude and a frequency range from 1 Hz to 1000 Hz, and analyzed the resulting waveforms for gain and phase shift. The analyzer was also used to test individual components and subsystems and thus obtain their open-loop transfer functions, which were then implemented in the model.

As an example of model validation, Figure 14 shows the response of the azimuth axis to a 30-deg step and compares it to the prediction from the simulation. The response is well behaved with little overshoot. The average slew rate from 0 to 100% of the commanded angle is 164 deg/sec.

### Performance Summary

Table 5 summarizes the performance of the final prototype in key areas.

The mass total is only for the mechanism and does not include the electronics, since the electronics are only breadboard at this stage of the development.

The average power was determined from the simulation by commanding both axes to perform continuous simultaneous slow scans, as would be used for GMC. The peak power was obtained by commanding both axes to do a large-angle step simultaneously.

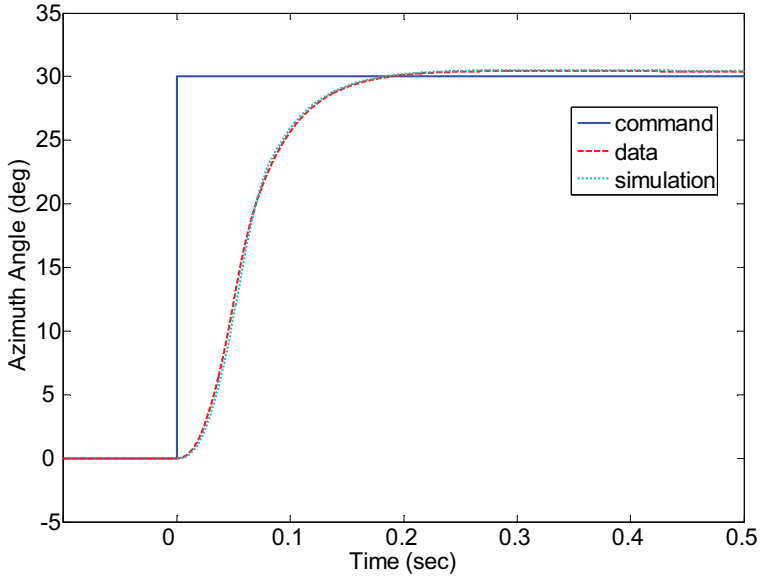


**Figure 14. Azimuth Axis Large-Angle Step Response**

**Table 5. Performance Specifications of Final Prototype**

| Specification | Value |
|---|---|
| Aperture (mm) | 75 |
| Mass (electronics not included) (kg) | 1.0 |
| Avg. Power (W) | 0.4 |
| Peak Power (W) | 30 |
| Azimuth Rot. (mechanical deg) | ±60 |
| Elevation Rot. (mechanical deg) | ±15 |
| Azimuth Error Mean (arcsec) | <1 |
| Azimuth Error Std. Dev. (arcsec) | <3 |
| Elevation Error Mean (arcsec) | <0.05 |
| Elevation Error Std. Dev. (arcsec) | <6.5 |
| Azimuth Slew Rate (0-100%) (deg/sec) | 160 |
| Elevation Slew Rate (0-100%) (deg/sec) | 75 |
| Bandwidth (Hz, 100 arcsec amplitude) | 70 |
| Gain Margin (dB) | 6 |

The error mean and standard deviations were calculated using the statistics of the angular position data at the end of a 10-second step-and-hold for both large and small steps. This is not absolute mirror pointing accuracy, but rather the tracking error between the commanded angle and the angle measured by the encoder for azimuth and the wedge sensor for elevation. Absolute pointing accuracy, as measured with the theodolite, was about 0.03 deg at room temperature.

The azimuth error is largely due to the limited counts of the encoder, 288000 counts over 360 deg of rotation, which results in 4.5 arcsec/count. The encoder toggles by one count during steady state, resulting in the error.

The elevation axis is extremely repeatable, as shown by the small mean error; however, the noise, represented by the error standard deviation, is larger than desired. The noise is attributed mainly to the 16-bit A/D computer card's peak-to-peak noise of over 15 counts, as claimed in the card manufacturer's specification sheet. This equates to about 25 arcsec of peak-to-peak noise, when the 16-bit resolution is applied to the full 30-deg mechanical angle of the elevation axis. Some noise is also generated by the wedge sensor electronics box. A digital moving average filter was applied to the wedge sensor feedback, which helped considerably. The control algorithm also contains a derivative term in the forward loop, which tends to enhance the noise.

The closed-loop bandwidth for each axis, as measured using the control systems analyzer, was about 70 Hz at the -3 dB point. The gain margin of 6 dB was verified by doubling the control algorithm gains in each axis and performing a step response test to determine that the system remained stable, which it did.

## FSM Portable Demonstration

Figure 15 shows the FSM portable demonstration system, which includes the FSM, the breadboard electronics, the host and target computers, and a laser for "light show" demonstrations. The system was programmed to project a Lissajous figure and an "S" figure on the ceiling at high frequencies, and also to do slow scans for audience visualization.

### Wedge Sensor Temperature Mapping

The current wedge sensor for feedback experiences drift with temperature, so a mapping was performed to show feasibility of achieving high absolute pointing accuracy. One possible application of the FSM requires a ±50-arcsec absolute pointing accuracy over a 0-40°C temperature range. The angle was measured using an autocollimator and mapped versus sensor voltage and temperature. Figure 16 shows that the results appear predictable and highly repeatable, verifying feasibility of mapping.

**Figure 15. Portable Demonstration**

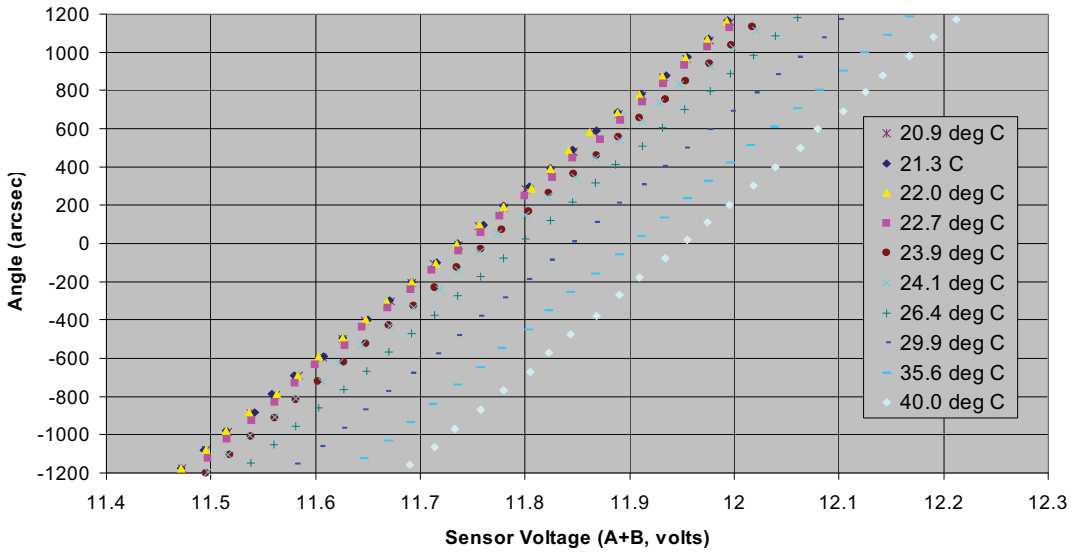


**Figure 16. Temperature Mapping**

## Launch Lock

Launch lock options included a permanent magnet, a shape-memory alloy pin-puller, and a wax actuator. The magnetic concept was chosen based on simplicity and a 6-year on-orbit heritage with another SDL scan mirror.

The patent-pending launch lock is shown in Figure 17. The combination of a magnet with a cone-shaped receptacle provides restraint in all directions. The restraint force is adjustable by changing the air gap, which is done by screwing the cup holding the magnet in or out and locking it with the set screw. The holding force is high enough to restrain motion during external loads, but is low enough that the actuator can overcome the holding force to release the lock. For this particular prototype, the latch force can be about 2.2 N maximum, since it is limited by the maximum current (~1 amp) and torque of the voice coil actuator. Analysis was performed to validate the design by applying the launch vibration spectrum to the dynamic model of the FSM shown in Figure 9.

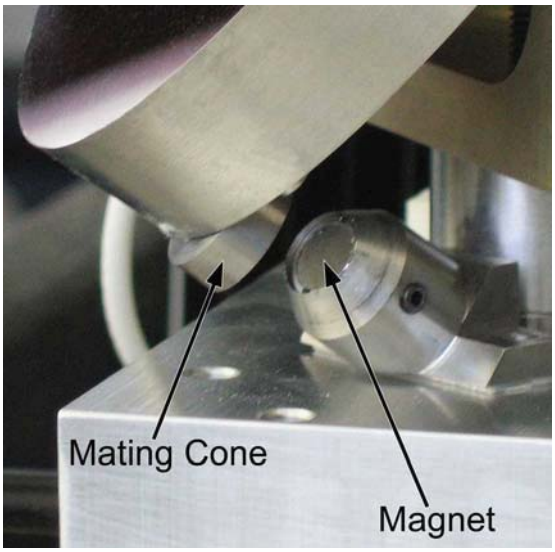


**Figure 17. Magnetic Launch Lock**

### Vibration Testing

A vibration test was conducted to verify the performance of the launch lock and the survivability of the FSM. The 3-minute test was based on proto-qualification levels for the planned STP-SIV spacecraft,

**Table 6. STP-SIV Spacecraft Vibration Spectrum**

| Frequency (Hz) | PSD – Acceptance (g2/Hz) | PSD – Protoqualification (g2/Hz) |
|---|---|---|
| 20 | 0.005 | 0.01 |
| 100 | 0.012 | 0.024 |
| 800 | 0.012 | 0.024 |
| 2000 | 0.005 | 0.01 |
| Overall (grms) | 4.27 | 6.04 |

shown in Table 6, with the first minute at reduced power and two minutes at full power. The test consisted of the following duty cycle:

- -12 db for 15 sec
- -9 db for 15 sec
- -6 db for 15 sec
- -3 db for 15 sec
- 0 db for 2 min.

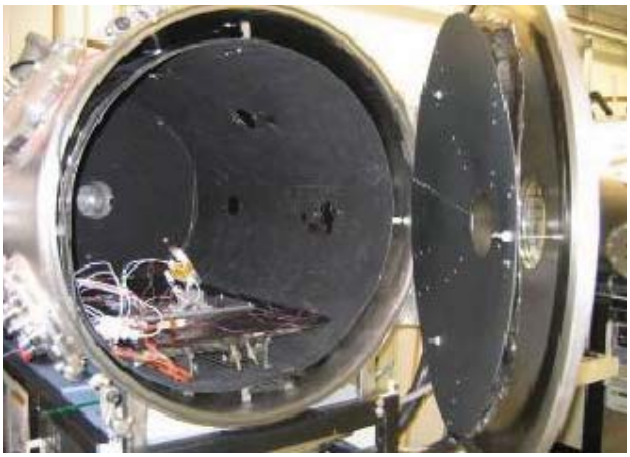

**Figure 18. FSM Mounted in Thermal Vacuum Chamber**

The launch lock magnetic force was set to about 1.5 N for the first vibe test. The launch lock released after 105 sec., but no violent mirror motions were observed. Measurement of the latch force after the test showed it to be about 1.4 N, so the set screw may have been loose. The latch force was increased to about 2.2 N for the second test. This test was successful. Before and after each test, the FSM was powered up and exercised with its nominal duty cycle of a Lissajous figure, an "S" figure, and slow scans. The performance appeared nominal before and after each test. The FSM was also repeatedly commanded to latch and unlatch positions, verifying that the voice coil could overcome the latch force.

## Thermal-Vacuum Testing

Although the FSM prototype was not intended for harsh testing, it was mounted in one of SDL's thermal-vacuum chambers (Figure 18) and subjected to 55 duty cycles with pressures as low as 1e-7 torr and temperatures to 164 K (the lower limit of the chamber's capability). The azimuth axis worked for 26 runs as the temperature dropped, until the thermocouple on the azimuth motor housing reached 227 K. This axis then ceased working as expected due to the bearing lube freezing up, since its published range is 233 K to 423 K. The elevation axis operated for all runs, down to 164 K. Figure 19 shows how the elevation axis "rings" at cold temperatures due to a change in the plant resulting in improper gains. The feedthrough cables add considerable noise, as shown for small angles in Figure 20. The azimuth noise was noticeably worse than the previous year, possibly due to bearing abuse during the vibe test, or loss of lubricant during vacuum testing. The encoder optics could also be impaired due to outgassing on the lens. Figure 21 shows how the "before" and "after" performance of the elevation axis at ambient for large angles is nearly identical. Some outgassing was evident from the residue collected in the chamber's cold trap, although it was not analyzed after testing.

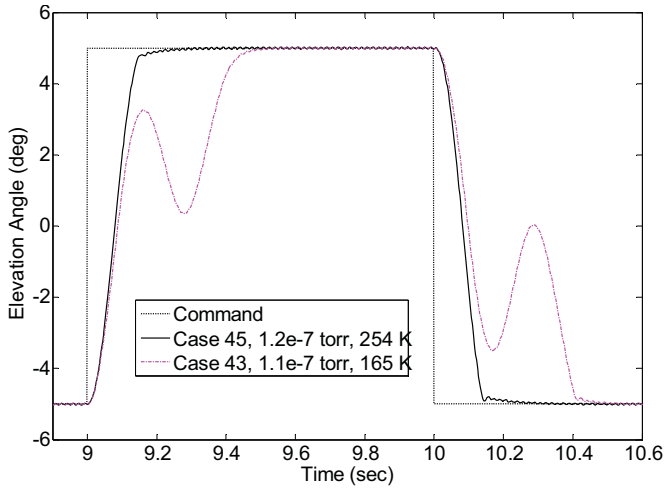


**Figure 19. Effect of Temperature on Elevation Step Response**

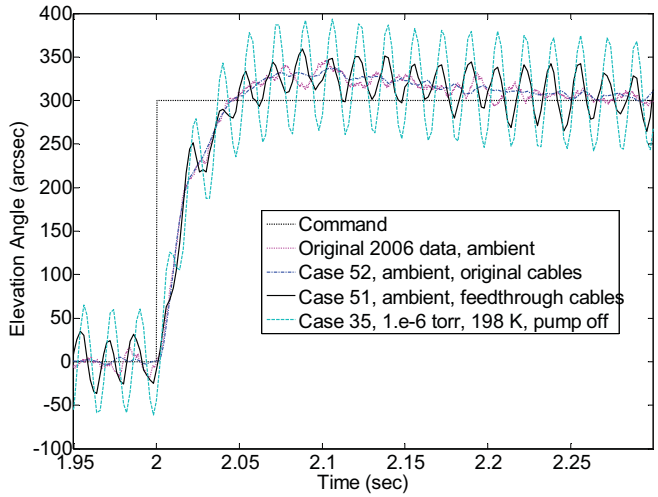


**Figure 20. Effect of Cable Noise on Elevation Small-Angle Response**

## Lessons Learned and Future Work

The FSM prototype has been shown through testing to have the potential for robust performance in the harsh environment of space. The elevation axis operates at hard vacuum and cold temperatures down to 164 K. The "before" and "after" ambient performance of the elevation axis is virtually the same. The azimuth axis works down to 233 K until the current bearing lube freezes up. The launch lock successfully handles a typical launch environment.

Obviously, some materials changes would need to be made for space and/or cryogenic applications. The azimuth lubricant would need to be changed. Also, the gains for both axes should be scheduled based on temperature. The cause and corrective action for the cable noise in both axes would need to be identified.

The elevation axis circuit design could be modified to allow a slightly higher current limit of about 2 amps to provide additional latch force and stall torque margins.

The focus of future efforts are being centered more on the development of space-type electronics, as described in the following paragraphs.

The control algorithms and filters need to be further refined and optimized to reduce the noise, especially in the elevation axis. This may be done by moving the derivative term to the feedback loop, using optimal state-space methods with observers, etc.

The algorithms need to be implemented in low-cost space-qualified processing hardware, such as an FPGA, DSP, or microprocessor. This may necessitate conversion to fixed-point math, as was done for the radiation-hardened fixed-point microprocessor used to control a FSM in another SDL space payload (Ref. 3).

A protocol or set of operational codes needs to be defined to communicate digitally with the FSM, such as commanding it to move to a position, querying it for the current position, etc.

The D/As, A/Ds, wedge sensor electronics, and quadrature encoder functionality need to be implemented using space-rated components.

The autocoding feature of the RPM process needs to be evaluated to determine how much of the code automatically generated for the control algorithms can be used in the final product.

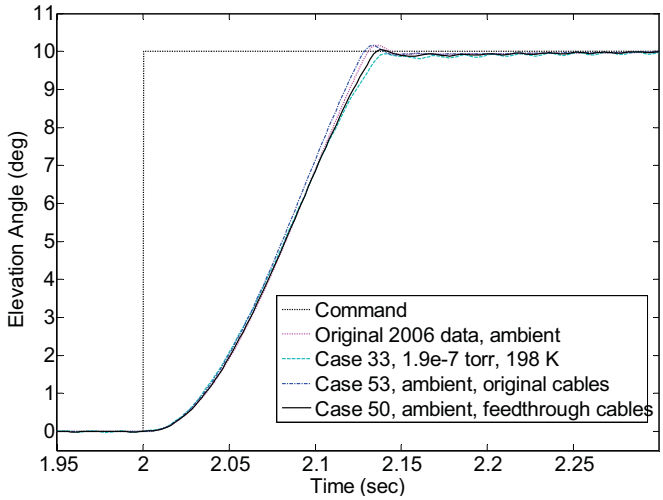


**Figure 21. Ambient Data for Elevation Angle Large-Step Response**

The input power interface needs to be defined to either use the spacecraft power to drive the motors or else have a customer supply the motor power.

Off-the-shelf space-rated three-phase motor amplifiers need to be evaluated.

It would also be desirable to develop an automated procedure for mapping the wedge sensor output against temperature and angle using optical techniques and precise temperature control.

## Summary

A low-cost two-axis FSM has been successfully developed and demonstrated for air- and space-based sensors. The 75-mm aperture mirror is lightweight, isolated by flexures, and maintains a surface figure of less than 0.1-wave RMS down to a temperature of 210 K. The drive system uses an innovative combination of off-the-shelf components to achieve large angles, high slew rates, high bandwidth, and relative position error less than 1 arcsec. A rapid prototyping methodology has been used to develop the control laws. Temperature mapping has been employed to improve the absolute pointing accuracy. A passive patent-pending launch lock has been developed and demonstrated. Vibration testing has been performed to show the survivability of the FSM and the successful operation of the launch lock. The mechanism has been subjected to many duty cycles in a hard vacuum and at low temperatures. Areas for improvement include a lower-temperature azimuth lubricant, gains scheduled with temperature, noise reduction in the cables, a higher elevation axis current limit, and development of space-worthy electronics.

## Acknowledgments

The authors express their sincere appreciation to the following individuals for their significant contributions: Richard Sanders and Melissa Draper, mechanical design; Trent Newswander, mirror design, analysis, and testing; Brent Jensen, structural analysis; Brian Thompson, trade studies and conceptual design; Steve Dansie, Andrew Little, and Scott Schicker, mechanical technologists; Duane Miles, optical technologist; Jeff Blakeley, analog and power electronics; James Cook and Zach Casper, electronics and software; Adam Shelley and Quinn Young, thermal design; Aaron Gilchrist, temperature mapping; and Jim Herrick, vacuum testing. The authors also appreciate the funding and support from the Research Division of SDL, directed by Dr. J. Steven Hansen and Dr. Scott Jensen.

## References

1. Steven R. Wassom, Morgan Davidson, Trent Newswander, James Cook, Zach Casper, Adam Shelley, “Fine Steering Mirror for Smallsat Pointing and Stabilization,” 20th Annual AIAA/USU Conference on Small Satellites, Paper #SSC06-VIII-7, 17 August 2006.

2. Ahmad, Anees, *Optomechanical Engineering Handbook*, CRC Press, 1999.

3. Steven R. Wassom, Chad Fish, Mitch Whiteley, Dave Russak, Joel Nelsen, Brian Thompson, Glen Hansen, Jason Wooden, Larry Gordley, John Burton, Mark Hervig, Paul Cucchiaro, Dan Hammerle, “SOFIE Pointing Control System,” SPIE Proceedings Vol. 6297, *Infrared Spaceborne Remote Sensing XIV*, 7 Sep. 2006.